



Phase relations in the Fe–FeSi system at high pressures and temperatures



Rebecca A. Fischer^{a,*}, Andrew J. Campbell^a, Daniel M. Reaman^a, Noah A. Miller^b,
Dion L. Heinz^a, Przymyslaw Dera^c, Vitali B. Prakapenka^c

^a Department of the Geophysical Sciences, University of Chicago, 5734 South Ellis Ave, Chicago, IL 60637, USA

^b Department of Geology, University of Maryland, College Park, MD 20742, USA

^c GeoSoilEnviroCARS, University of Chicago, 5640 South Ellis Ave, Chicago, IL 60637, USA

ARTICLE INFO

Article history:

Received 7 September 2012

Received in revised form

22 April 2013

Accepted 23 April 2013

Editor: L. Stixrude

Available online 30 May 2013

Keywords:

high pressure
iron–silicon alloys
phase diagrams
Earth's core

ABSTRACT

The Earth's core is comprised mostly of iron and nickel, but it also contains several weight percent of one or more unknown light elements, which may include silicon. Therefore it is important to understand the high pressure, high temperature properties and behavior of alloys in the Fe–FeSi system, such as their phase diagrams. We determined melting temperatures and subsolidus phase relations of Fe–9 wt% Si and stoichiometric FeSi using synchrotron X-ray diffraction at high pressures and temperatures, up to ~200 GPa and ~145 GPa, respectively. Combining this data with that of previous studies, we generated phase diagrams in pressure–temperature, temperature–composition, and pressure–composition space. We find the B2 crystal structure in Fe–9Si where previous studies reported the less ordered bcc structure, and a shallower slope for the hcp+B2 to fcc+B2 boundary than previously reported. In stoichiometric FeSi, we report a wide B2+B20 two-phase field, with complete conversion to the B2 structure at ~42 GPa. The minimum temperature of an Fe–Si outer core is 4380 K, based on the eutectic melting point of Fe–9Si, and silicon is shown to be less efficient at depressing the melting point of iron at core conditions than oxygen or sulfur. At the highest pressures reached, only the hcp and B2 structures are seen in the Fe–FeSi system. We predict that alloys containing more than ~4–8 wt% silicon will convert to an hcp+B2 mixture and later to the hcp structure with increasing pressure, and that an iron–silicon alloy in the Earth's inner core would most likely be a mixture of hcp and B2 phases.

© 2013 Elsevier B.V. All rights reserved.

1. Introduction

Earth's core is an iron-rich alloy containing some nickel and several weight percent of elements lighter than iron (Birch, 1952). This light element component is likely a mixture of silicon, oxygen, sulfur, carbon, and/or hydrogen (e.g., Allègre et al., 1995; McDonough, 2003; Poirier, 1994). Understanding phase relations in systems containing iron and one or more light elements is critical for deducing the composition and structure of the Earth's core. Binary phase diagrams are a necessary step before more realistic phase diagrams containing two or more light elements can be studied. Extrapolations of high pressure–temperature (P – T) phase diagrams allow prediction of the crystal structure of the inner core, which may help explain its observed anisotropy (e.g., Deguen, 2012; Mattesini et al., 2010; Stixrude and Cohen, 1995). Phase diagrams reveal which phases' equations of state and other properties should be compared to those of the core (e.g., Fischer

et al., 2011). In this study, we determine the phase diagrams of iron–silicon alloys. Estimates of the core's maximum silicon content vary, ranging from less than 4 wt% (Antonangeli et al., 2010), to ~6–7 wt% (Allègre et al., 1995; Brosh et al., 2009; Javoy et al., 2010; McDonough, 2003; Shahar et al., 2009), to 8–12 wt% (Alfè et al., 2002; Asanuma et al., 2011; Fischer et al., 2012; Lin et al., 2003; Ricolleau et al., 2011; Rubie et al., 2011), to up to 20 wt% (Balchan and Cowan, 1966; Ringwood, 1959), based on a wide range of experimental and modeling techniques.

Pure iron has the hexagonal close-packed (hcp) structure at Earth's inner core conditions (Tateno et al., 2010), but the effects of light elements need to be studied systematically as a function of composition. Some work has previously been done on high P – T phase diagrams of iron–silicon alloys. Fischer et al. (2012) studied the subsolidus phase relations and melting curve of Fe–16 wt% Si alloy (Fe–16Si) to 140 GPa (Fig. 1). Asanuma et al. (2008) investigated Fe–3.4Si, finding a mixture of face-centered cubic (fcc) and hcp structures, and only the hcp structure at lower temperatures and higher pressures. Sakai et al. (2011) studied Fe–4.8Ni–4.0Si, finding only the hcp structure at pressures above ~150 GPa. Lin et al. (2002, 2009) studied Fe–7.9Si, discovering a mixture of fcc

* Corresponding author. Tel.: +1 773 834 1085; fax: +1 773 702 9505.
E-mail address: rfischer@uchicago.edu (R.A. Fischer).

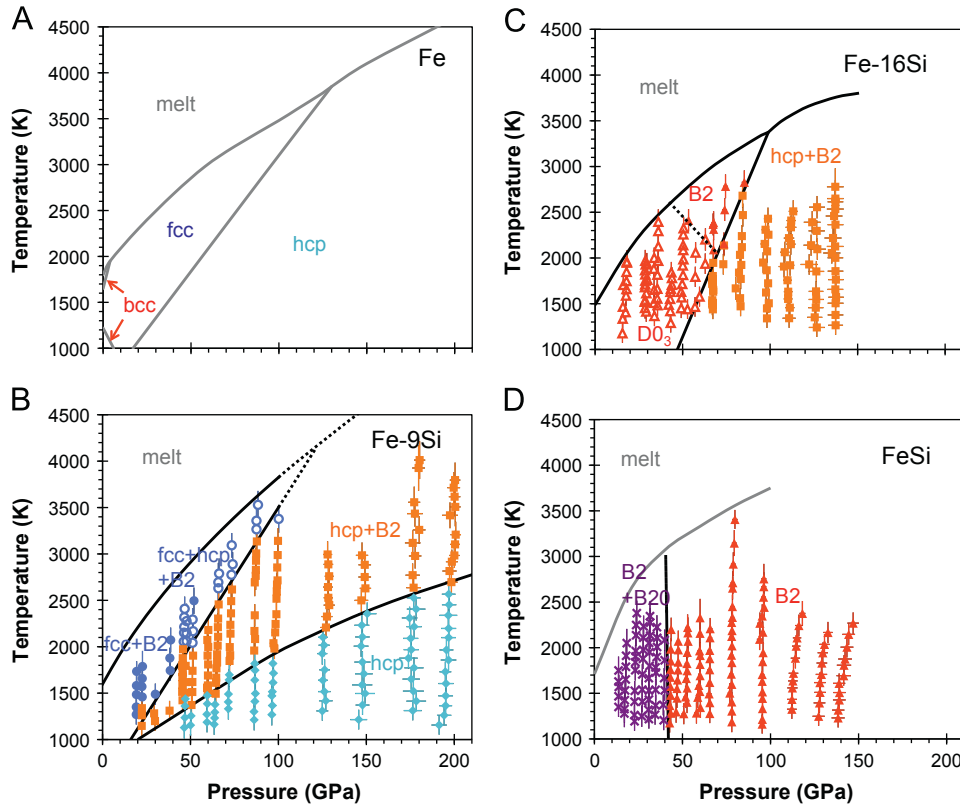


Fig. 1. Pressure–temperature phase diagrams in the Fe–FeSi system for various compositions. (A) Phase diagram of pure Fe. Subsolidus phase boundaries are taken from Komabayashi and Fei (2010), and the melting curve is from Ma et al. (2004). (B) Phase diagram of Fe–9Si, this study. Filled blue circles: fcc+B2. Open blue circles: metastable fcc+hcp+B2. Orange squares: hcp+B2. Teal diamonds: hcp. (C) Phase diagram of Fe–16Si, from Fischer et al. (2012). Open red triangles: D0₃ structure. Filled red triangles: B2. (D) Phase diagram of FeSi, this study. Gray line: melting curve of Lord et al. (2010). Purple × s: B2+B20. (For interpretation of the references to color in this figure legend, the reader is referred to the web version of this article.)

and body-centered cubic (bcc) structures at low pressures and high temperatures, hcp+bcc at intermediate pressures, and hcp at the highest pressures. Hirao et al. (2004) performed room temperature compression on Fe–8.7Si, finding a conversion from bcc to hcp structures at 16–36 GPa, consistent with results of Lin et al. (2003) on Fe–7.9Si. Kuwayama et al. (2009) investigated the phase diagrams of Fe–9.9Si and Fe–6.4Si, while Zhang and Guyot (1999a, 1999b) studied Fe–8.9Si.

Stoichiometric FeSi is known from quench studies and theory to transform from the B20 (FeSi-type) structure to the B2 (CsCl-type) structure at higher pressures (Caracas and Wentzcovitch, 2004; Dobson et al., 2002, 2003; Lord et al., 2010; Vočadlo et al., 1999), but the location and slope of this boundary have been uncertain. Guyot et al. (1997) and Whitaker et al. (2008, 2009) report thermal equations of state and elastic properties of B20–FeSi, respectively. Knittle and Williams (1995) and Lin et al. (2003) compressed B20–FeSi at 300 K, while Dobson et al. (2003), Sata et al. (2010), and Ono et al. (2007) studied compression of B2–FeSi at 300 K. The melting curve of FeSi was measured by Lord et al. (2010) and Santamaría-Pérez and Boehler (2008). Melting curves of other Fe–Si alloys have also been studied (Asanuma et al., 2010; Morard et al., 2011; Fischer et al., 2012). Phase relations in the Fe–FeSi system were reported by Massalski (1986) at 1 bar, and by Kuwayama and Hirose (2004) at 21 GPa. The system has also been studied computationally (e.g., Brosh et al., 2009; Côté et al., 2010; Zhang and Oganov, 2010).

In various studies, different compositions of Fe–Si alloys have been reported to have the bcc, B2, and D0₃ crystal structures, which are highly related. The B2 structure is an ordered version of the bcc structure, containing two sites in equal abundance. In Fe–Si alloys with the B2 structure, one of the sites is preferentially

occupied by Fe and the other site is preferentially occupied by Si. The D0₃ structure can be thought of as a doubling of the B2 unit cell in each direction, with a higher degree of ordering. Again, in Fe–Si alloys with the D0₃ structure, iron atoms will prefer one site and Si atoms will prefer the other site. There cannot be perfect ordering in Fe–Si alloys unless the stoichiometry precisely matches the structure (FeSi for the B2 structure, Fe₃Si for the D0₃ structure), but the alloys may be partially ordered, with Fe and Si atoms showing a site preference.

In this study, we determine the high *P–T* phase diagrams of Fe–9Si and FeSi, using synchrotron X-ray diffraction in a laser-heated diamond anvil cell, up to pressures and temperatures approaching those of Earth's outer core. We synthesize our results with other recent studies on the Fe–FeSi system to determine how phase relations in this system evolve as a function of pressure, temperature, and composition. This allows prediction of the crystal structure of the Earth's inner core and identification of the phase(s) whose properties are most relevant to the inner and outer core, assuming a predominantly Fe–Si core. These phase diagrams can be applied to studies of other planetary cores, and will serve as a basis for future studies on multi-component systems of candidate core materials.

2. Experimental methods

The Fe–9Si starting material (Goodfellow Corporation) was analyzed by electron microprobe (Miller, 2009) and found to be chemically homogeneous, containing 8.75 ± 0.40 wt% silicon (Fe_{0.84}Si_{0.16} by mole, hereafter Fe–9Si). Fe–9Si or stoichiometric FeSi (Alfa Aesar) was pressed in a diamond cell to produce a foil

~3–5 μm thick. Rhenium gaskets, initially 250 μm thick, were preindented to 25–30 GPa, then a hole up to 100 μm in diameter was machined in the center of the indentation to serve as the sample chamber. The diamond anvils had 300 or 400 μm culets, or they were beveled, with 120, 150, or 250 μm flats and an 8° bevel out to 300 μm . Sample foils were loaded into a diamond anvil cell between two layers of KBr, each ~10 μm thick. A few experiments on the melting curve of Fe–9Si were loaded in NaCl instead of KBr. The KBr (or NaCl) served as the pressure medium, thermal insulator, and pressure standard. The entire sample assembly was oven-dried at ~90 °C for approximately 1 h after cell loading but before the cell was closed to remove any moisture.

Laser-heating angle-dispersive X-ray diffraction experiments were performed at beamline 13-ID-D (GeoSoilEnviroCARS) of the Advanced Photon Source (APS) at Argonne National Laboratory (Prakapenka et al., 2008; Shen et al., 2005). The incident X-ray beam was monochromatic ($\lambda=0.3344$ Å) and measured ~4 $\mu\text{m} \times 4$ μm . Diffracted X-rays were collected using a MAR165 CCD detector, with exposure times of 5 s. Sample-to-detector distance was calibrated by 1 bar diffraction of CeO₂. The diffraction patterns were integrated to produce 2θ plots using Fit2D (Hammersley et al., 1996), then peak fitting of the integrated patterns was performed using PeakFit (Systat Software). The 2D diffraction images were also examined for evidence of small diffraction peaks that indicate ordering of the alloy phases.

Pressures were determined from the volume of the pressure standard and its temperature using the thermal equation of state of KBr (or NaCl) in the B2 structure (Fei et al., 2007; Fischer et al., 2012). The lattice parameter of KBr and its uncertainty were determined as the average and standard error of 4–13 d -spacings. Uncertainties in pressure were derived from uncertainties in temperature and lattice parameter. The KBr temperature during laser-heating was less than the measured sample temperature, due to axial thermal gradients through the insulator, so the KBr temperature was corrected downward following Campbell et al. (2009). By using KBr as the pressure standard, we assume that the sample and pressure medium are in mechanical equilibrium.

The sample was laser-heated by 1064 nm Yb fiber lasers with “flat top” profiles created by pi-shaping optics, with the laser power on each side being independently adjustable to allow minimization of axial temperature gradients through the sample (Prakapenka et al., 2008). Diffraction patterns were collected on heating and cooling. Temperatures were determined by spectro-radiometry (Heinz and Jeanloz, 1987) using the graybody approximation, and were measured simultaneously with the diffraction patterns. Laser-heated spots were ~20 μm in diameter, much larger than the X-ray beam to minimize radial temperature gradients in the region probed by X-rays. Temperatures were simultaneously measured on the upstream and downstream sides of the sample from an area 5 μm in diameter in the center of the laser-heated spot, comparable to the size of the X-rayed region. X-ray-induced fluorescence of KBr was used to align the optical axes of the laser heating and temperature measurement system with the X-ray beam. Upstream and downstream temperatures were averaged to obtain the measured sample temperature. For subsolidus measurements, the measured temperatures were then corrected downward by 3% to estimate the sample temperature, accounting for a small axial temperature gradient through the sample (Campbell et al., 2007, 2009). Reported temperature uncertainties include an analytical uncertainty of 100 K from the temperature measurement system (Shen et al., 2001), the difference between the upstream and downstream temperatures, and uncertainty from the correction for the thickness of the sample (Campbell et al., 2007, 2009).

Temperature measurements in the diamond cell were benchmarked by analyzing a sample of iron in an MgO pressure medium

to check the location of the hcp–fcc transition in iron (Fischer et al., 2011, 2012). The sample was compressed to ~45 GPa based on the equation of state of hcp-Fe (Dewaele et al., 2006) and laser-heated. The phase transition was bracketed between volumes and temperatures of 5.862 ± 0.026 cm³/mol (hcp volume), 1769 ± 120 K; and 6.039 ± 0.021 cm³/mol (fcc volume), 1820 ± 109 K. These values agree with the published phase diagram of Komabayashi and Fei (2010).

Samples for room temperature compression were loaded in a quasi-hydrostatic neon pressure medium using the COMPRES/GSECARS gas-loading system at the APS (Rivers et al., 2008). The sample was loaded with a few grains of KBr and ruby for pressure standards (Fischer et al., 2012; Mao et al., 1986). Room temperature compression of FeSi was performed at the APS, while compression of Fe–9Si was done at beamline 12.2.2 of the Advanced Light Source (ALS), Lawrence Berkeley National Laboratory (Kunz et al., 2005). At the ALS, LaB₆ was used to calibrate the sample-to-detector distance. A MAR345 image plate or Bruker CCD detector was used, with a monochromatic incident beam ($\lambda=0.41323$ Å) measuring 30 $\mu\text{m} \times 30$ μm . Exposure times at the ALS were typically 20 s.

3. Results

3.1. Fe–9Si phase diagram

We determined the high P – T phase diagram of Fe–9Si to 200 GPa and over 4000 K, as shown in Fig. 1b (the phase diagram of pure iron is shown in Fig. 1a for comparison). This alloy has the DO₃ crystal structure at ambient conditions (Massalski, 1986) and under compression at 300 K to 29 GPa. The DO₃ structure, with space group $Fm\bar{3}m$, was previously reported for Fe–16Si (Fischer et al., 2012) and for Fe–5Ni–10Si (Morard et al., 2011). At high pressures and temperatures, the Fe–9Si alloy took on the hcp structure. With increasing temperature, it converted to an hcp+B2 mixture, then to fcc+B2. At the highest temperatures, sometimes three phases (fcc+hcp+B2) were present in the experiments. The P – T data and the phase(s) observed are recorded in Supplementary Table S1.

Fig. 2 shows two diffraction patterns of Fe–9Si in KBr. The lower pattern was collected at 30 GPa and 1490 K on heating, with peaks corresponding to B2 KBr, fcc Fe–9Si, and B2 Fe–9Si. The alloy is shown to have the B2 structure, and not the bcc structure as previously reported (Lin et al., 2002, 2009), due to the presence of the 111 peak. The upper pattern in Fig. 2 was collected on a different sample of Fe–9Si at 87 GPa and 2760 K, also on heating. All observed peaks correspond to B2 KBr, hcp Fe–9Si, or B2 Fe–9Si. In this pattern, the 100 peak of B2 Fe–9Si is visible, indicating that the alloy has the B2 (not bcc) structure. Supplementary Fig. S1 shows a series of diffraction patterns at ~200 GPa. The B2 peaks appear on heating and increase in intensity with progression into the two-phase loop as the temperature is raised.

We measured high pressure melting of Fe–9Si, based on the appearance of diffuse X-ray scattering from the liquid alloy with increasing temperature (e.g., Dewaele et al., 2007; Fischer et al., 2012; Morard et al., 2008, 2011). Fig. 3 shows an example of diffuse scattering during laser heating at ~74 GPa. These diffraction patterns were all obtained with the same exposure time, and they were offset (by < 1%) to match intensities at $2\theta=5.0^\circ$. Beginning at 3390 K, a broad elevated bump in the background appears at approximately $2\theta=8$ – 12° , due to X-ray scattering by the liquid. The diffuse scattering intensity increases with increasing temperature, indicating a higher fraction of partial melt. Peaks from one phase persist with the liquid while peaks from the other phase shrink when diffuse scattering appears, indicating eutectic

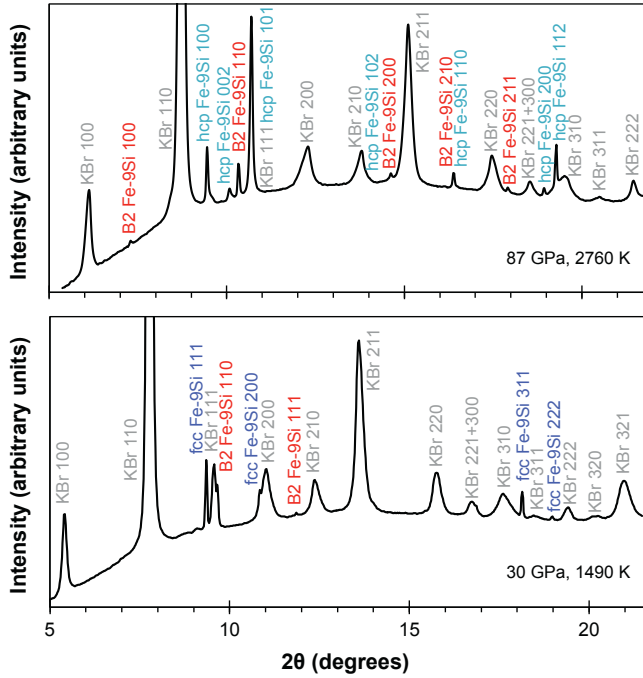


Fig. 2. Diffraction patterns of Fe–9Si, showing different phase assemblages. Data were collected on heating. Lower: pattern collected at 30 GPa and 1490 K, with peaks corresponding to B2 KBr, fcc Fe–9Si, and B2 Fe–9Si. Upper: pattern collected at 87 GPa and 2760 K, with peaks corresponding to B2 KBr, hcp Fe–9Si, and B2 Fe–9Si. The 100 and 111 peaks of B2 Fe–9Si indicate that the alloy has the B2 (not bcc) structure.

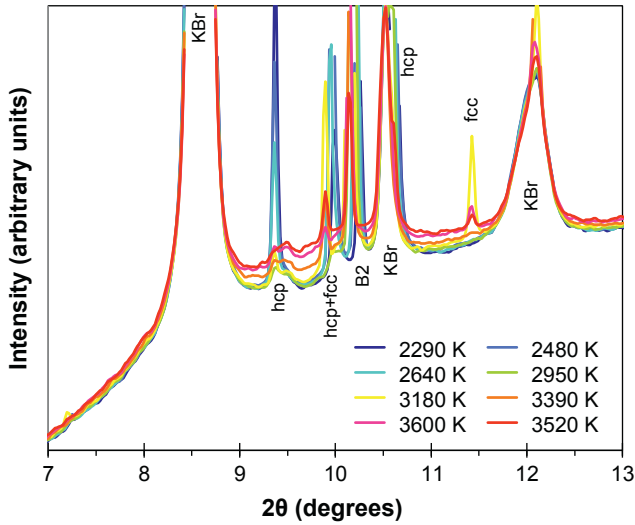


Fig. 3. Diffuse X-ray scattering, indicating melting of Fe–9Si alloy at ~ 74 GPa. An elevated background appears between $2\theta = 8\text{--}12^\circ$ ($Q \sim 33 \text{ nm}^{-1}$) at temperatures between 3180 K and 3390 K, bracketing the melting point. This signal continues to increase with increasing temperature, indicating a higher fraction of partial melt. Metastable hcp peaks diminish rapidly with increasing temperature. Upon melting, B2 peaks persist while fcc peaks shrink, indicating that B2 is the liquidus phase for Fe–9Si at this pressure.

melting. Pressures and temperatures of bounds on melting from X-ray diffuse scattering are listed in [Supplementary Table S2](#).

We also detected melting by analyzing the relationship between laser power and temperature in cases where laser power data were recorded during the experiment, to compare to the data on diffuse scattering. [Fig. 4](#) illustrates this relationship for two heating cycles on Fe–9Si, at ~ 88 GPa and ~ 101 GPa. Below the melting point, temperature increases monotonically and linearly

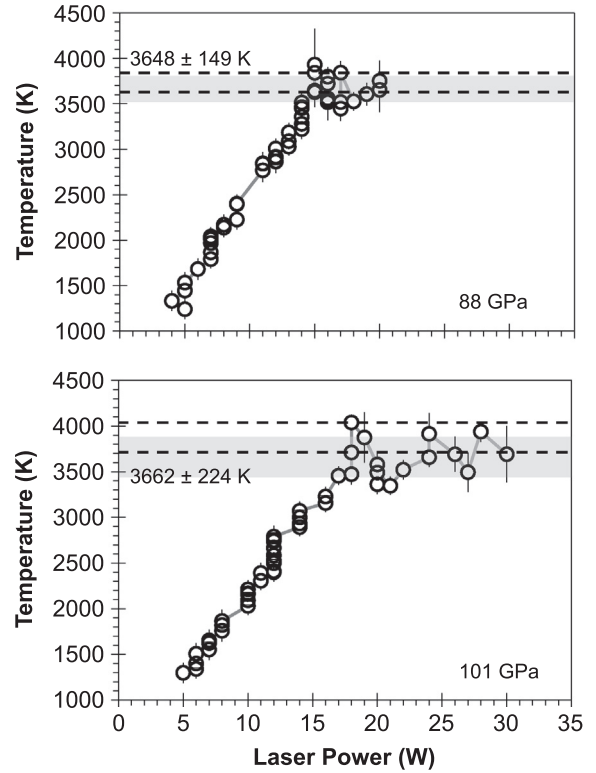


Fig. 4. Laser power–temperature relationships during two heating cycles on Fe–9Si. Upper: heating cycle at ~ 88 GPa. Lower: ~ 101 GPa. Below the melting point, temperature increases linearly and monotonically with laser power; once the melting point is reached, the temperature fluctuates around a plateau as laser power is increased further. Shaded gray regions indicate the melting point with width showing uncertainty. Laser powers are rounded to the nearest whole number. Black dashed lines indicate the bounds on the melting temperature from X-ray diffuse scattering during the same experiments.

with laser power, then there is a discontinuity at the melting temperature. As laser power is increased further, the temperature plateaus, fluctuating unstably around the melting point. The melting temperature is taken as the average of temperatures within the plateau ([Lord et al., 2010](#)), with its uncertainty calculated as the standard deviation of these values. Pressures and temperatures of melting from laser power–temperature discontinuities are reported in [Supplementary Table S3](#).

3.2. FeSi phase diagram

We determined the high P – T phase diagram of stoichiometric FeSi to ~ 145 GPa and over 3400 K, as shown in [Fig. 1d](#). FeSi is stable in the B20 structure at ambient conditions. It maintained the B20 structure under room temperature compression to ~ 36 GPa. At high temperatures between 14 GPa and 42 GPa a two-phase region was observed, with coexisting B2 and B20 structures. [Fig. 5](#) shows a diffraction pattern of FeSi in KBr collected at 39 GPa and 1210 K. It shows coexistence of the B2 and B20 structures of FeSi under these conditions.

From 42 GPa to 145 GPa, the highest pressure reached in this study for this composition, FeSi maintained the B2 structure ([Fig. 1d](#)). A single melting experiment was performed on FeSi, at ~ 80 GPa. The melting point was bracketed between 3410 K and 3610 K, based on the appearance of diffuse scattering in the X-ray diffraction pattern. The P – T data and the corresponding phase(s) observed in FeSi are recorded in [Supplementary Table S4](#).

4. Discussion

4.1. Fe–9Si subsolidus phase diagram

Recent studies on compositions similar to Fe–9Si (Hirao et al., 2004; Lin et al., 2003; Zhang and Guyot, 1999a, 1999b) did not report the DO_3 structure at ambient conditions or under room temperature compression, possibly because it is an ordered version of the bcc structure, and the diffraction peaks indicating this ordering are small and difficult to detect (Fischer et al., 2012). While we observed this structure to 29 GPa at room temperature, other studies reported a gradual transition to the hcp structure beginning at 16 GPa (Hirao et al., 2004; Lin et al., 2003). This difference may be due to slow kinetics at room temperature, with an even more sluggish transformation expected under the more hydrostatic conditions used in the present study. Due to this kinetic effect, we were unable to constrain the P – T conditions under which the DO_3 structure is the equilibrium phase.

Silicon partitions between coexisting phases, as discussed in Section 4.4 and in previous studies (Kuwayama et al., 2009; Lin et al., 2002). Our phase diagram is generally consistent with those reported by Lin et al. (2002, 2009) and Kuwayama et al. (2009) for Fe–7.9Si and Fe–9.9Si, respectively, but with several minor differences. First, we observe the B2 structure at high P – T conditions where Lin et al. (2002, 2009) reported the bcc structure. It may be technological advances in sample preparation and data analysis that permitted the detection of B2 ordering in the present study. Second, our phase boundary between hcp+B2 and fcc+B2 has a different slope from that of Lin et al. (2002). We find a slope of ~ 28 K/GPa, while the earlier study found a steeper slope of ~ 52 K/GPa. Our phase boundary will intersect the melting curve at ~ 110 GPa.

Third, our phase boundary between hcp and hcp+B2 diverges from that of Lin et al. (2002, 2009) at pressures below ~ 55 GPa. Lin et al. (2002, 2009) reported a highly curved phase boundary to match the transition at 300 K (Lin et al., 2003). We do not report a curved phase boundary, because it implies that the phase(s) on one side of the boundary has a very different compressibility than the phase(s) on the other side (such as solid and melt), which is unlikely for different structures of iron–silicon alloy. There may be a kink in the phase boundary instead of a curve, due to complexities of the phase diagram at lower pressures. Lin et al. (2003) may have also overestimated the transition pressure at 300 K due to kinetic hindrance of the transition. Kuwayama et al. (2009) report a similar slope for the hcp to hcp+B2 phase boundary as in the present study, though slightly steeper and shifted upward by a few hundred degrees. The appearance and disappearance of phases are difficult to detect near phase boundaries, sometimes requiring close examination of the 2D diffraction image rather than the integrated pattern, making it possible that Kuwayama et al. (2009) overestimated the transition temperature. This study, Lin et al. (2009), and Kuwayama et al. (2009) report fairly similar hcp to hcp+B2 phase boundaries where well-constrained by data, though they differ in their extrapolations to core pressures (Section 4.5; Fig. S2).

At high temperatures, we sometimes observe coexisting fcc+hcp+B2 phases instead of fcc+B2, which may represent slow kinetics in the disappearance of the hcp structure. An analogous transition occurs in pure iron, in which hcp iron commonly persists at temperatures above the hcp–fcc phase boundary (e.g., Komabayashi et al., 2009), lending support to this explanation. A three-phase region is forbidden by Gibbs' phase rule, so it is not the equilibrium assemblage. It could have been caused by a thick sample supporting a large axial temperature gradient, but our samples were very thin. It could also be caused by diffusion of carbon into our sample (Prakapenka et al., 2003), allowing for

a third equilibrium phase, though we see no evidence of carbides in our diffraction patterns. An identical three-phase assemblage was seen by Lin et al. (2002) in an alloy of similar composition, suggesting a problem with kinetics rather than sample preparation. Furthermore, in Fischer et al. (2012), we performed identical experiments on Fe–16Si, and saw no effects of temperature gradients in crossing the hcp+B2 to DO_3 phase boundary, again suggesting a kinetic problem in this case. The hcp diffraction peaks rapidly decay in intensity after crossing into the fcc+B2 field (Fig. 3).

4.2. Fe–9Si melting

The high pressure melting curve of Fe–9Si is illustrated in Fig. 6. There is good agreement between data obtained from diffuse scattering and from laser power–temperature discontinuities. To extrapolate the melting curve, we fit the data to the Simon

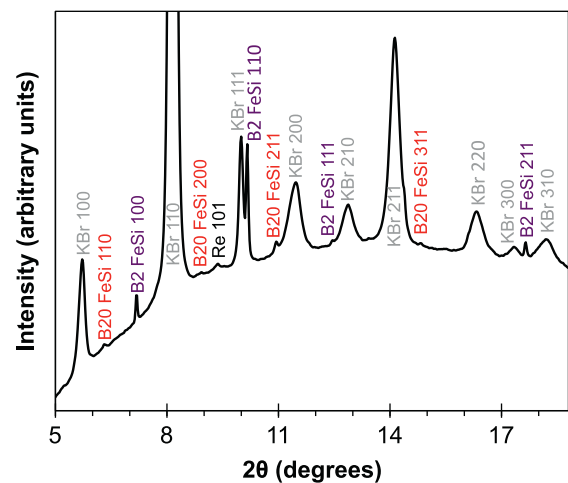


Fig. 5. X-ray diffraction pattern of FeSi collected at 39 GPa and 1210 K. Peaks correspond to B2 KBr, B20 FeSi, and B2 FeSi, with one faint peak from the rhenium gasket.

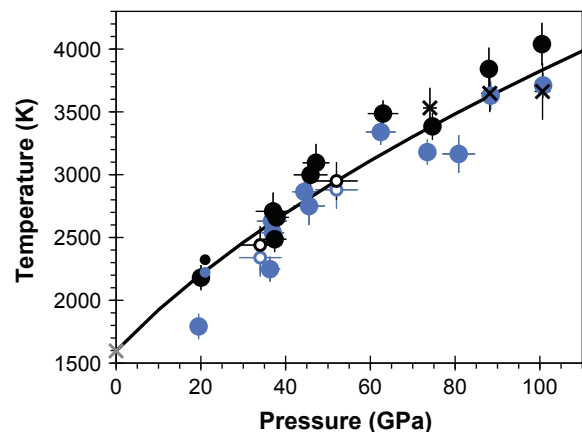


Fig. 6. High pressure melting curve of Fe–9Si: lower bounds (filled blue circles) and upper bounds (filled black circles) on melting temperatures from X-ray diffuse scattering. Black \times s: melting points from laser power–temperature relationships. Gray \times : 1 bar melting point, from Massalski (1986). Small solid blue and black circles (at 21 GPa): lower and upper bounds on melting, respectively, from Kuwayama and Hirose (2004). Small open blue and black circles (34 and 52 GPa): lower and upper bounds on melting of Fe–5Ni–10Si (Morard et al., 2011). Black line: the Simon equation fit to the data of this study. (For interpretation of the references to color in this figure legend, the reader is referred to the web version of this article.)

equation, $T_m = T_{ref}([P_m - P_{ref}]/a + 1)^{1/c}$, where T_m and P_m are the temperature and pressure of melting; T_{ref} and P_{ref} are a reference temperature and pressure of melting, respectively, set equal to the melting point at one bar; and a and c are fitted parameters (Simon and Glatzel, 1929). We fit both the data obtained by the laser power–temperature method and by the diffuse scattering method, averaging each set of upper and lower bounds. Using an unweighted least squares routine, we find $a = 23.6$ and $c = 1.89$. The Simon equation fit to our data is shown in Fig. 6.

Kuwayama and Hirose (2004) measured melting in the Fe–FeSi system at 21 GPa, including experiments on Fe–10Si that agree with our results on Fe–9Si (Fig. 6). Morard et al. (2011) bracketed melting points of Fe–5Ni–10Si using X-ray diffuse scattering at 34 GPa and 52 GPa (Fig. 6), also consistent with our results. In some cases we could identify which solid phase coexisted with the melt (the liquidus phase) in Fe–9Si (Supplementary Table S2). At pressures of 20–63 GPa, the liquidus phase has the fcc structure, while from 74 to 101 GPa, it has the B2 structure.

4.3. FeSi phase diagram

This study represents the highest pressure to which FeSi has been investigated with in situ X-ray diffraction in a laser-heated diamond anvil cell. Therefore, the present study more accurately reflects the equilibrium phase assemblage of FeSi than previous studies, in which samples were quenched from high temperatures (Lord et al., 2010), or from both high temperatures and pressures (Dobson et al., 2002), or were only compressed at 300 K (Dobson et al., 2003; Ono et al., 2007; Sata et al., 2010).

We observed the B20 structure in FeSi to at least 36 GPa at room temperature, but this may not accurately represent its stability field due to slow transition kinetics at 300 K. In our lowest pressure laser-heating experiments (~ 14 GPa), we observed a B2+B20 mixture over all temperatures investigated, with this mixture stable to ~ 42 GPa at high temperatures. This is consistent with many, but not all, earlier data on the FeSi phase diagram, in which a B2+B20 mixture was often quenched (Dobson et al., 2002; Lord et al., 2010). While these data were usually interpreted as a back-conversion from the B2 structure to the B20 structure upon quench or polishing (Dobson et al., 2002), our results demonstrate that a wide two-phase loop exists in the FeSi phase diagram. We observe coexisting phases over an extensive pressure–temperature range, and our samples were sufficiently thin that the observation of two phases cannot be attributed to temperature gradients within the sample. The two-phase assemblage was seen in seven distinct heating and cooling cycles on multiple samples. Relative proportions of the two phases change across this region, with X-ray diffraction patterns dominated by B20 peaks at lower pressures and by B2 peaks as the pressure approached 42 GPa (e.g., Fig. 5), consistent with a two-phase loop. Frequently one phase was only visible in the 2D diffraction image as a few faint reflections, too weak to appear in the integrated pattern. This may explain why earlier studies (Dobson et al., 2002, 2003; Lord et al., 2010) sometimes report only one phase in this region of P – T space.

At higher pressures, FeSi converts to the B2 structure only (Fig. 1d), as reported in previous experimental studies (Dobson et al., 2002, 2003; Lord et al., 2010) and predicted theoretically (Vočadlo et al., 1999). We did not cross this phase boundary in any heating cycle, so it must be very steep (slope of greater than approximately ± 180 K/GPa) and located at ~ 40 – 43 GPa, notably steeper and at a higher pressure than previously reported for a direct B20-to-B2 transition (Lord et al., 2010). FeSi has the B2 structure to at least ~ 145 GPa, the highest pressure reached for this composition, in agreement with calculations (Brosh et al., 2009; Zhang and Oganov, 2010). We have extended the subsolidus phase

diagram to higher pressures than previous high-temperature experimental studies, which reached maximum pressures of 35–40 GPa (Dobson et al., 2003; Lord et al., 2010). Lin et al. (2003) performed a single laser-heating X-ray diffraction experiment on FeSi at 2219 K and 54 GPa and reported the B20 structure, which is inconsistent with our results and with other experimental studies (Dobson et al., 2002; Lord et al., 2010).

We performed one melting experiment on FeSi at ~ 80 GPa, finding agreement with the melting curve of Lord et al. (2010) (Fig. 1d), which was based on discontinuities between laser power and temperature. However, the melting curve of Santamaría-Pérez and Boehler (2008), based on changes in sample texture determined by shining a laser on the sample, lies ~ 500 K lower. This lower melting curve conflicts with our result at 80 GPa and some of our experiments at lower pressures (e.g., at ~ 24 GPa), in which we reached temperatures above the melting curve of Santamaría-Pérez and Boehler (2008) but did not observe melting.

4.4. Phase diagrams in the Fe–FeSi system

Fig. 1 illustrates pressure–temperature phase diagrams in the Fe–FeSi system with varying silicon contents. The addition of Si stabilizes B2 and related structures in the Fe–FeSi system, whereas increasing pressure promotes stability of the hcp structure. This suggests that at pressures higher than those achieved in Fischer et al. (2012) and the present study, Fe–16Si and FeSi might eventually also transform to the hcp structure. The fcc structure was only observed in two-phase fields in Fe–FeSi alloys, and only those with low silicon contents (Asanuma et al., 2008; Fig. 1b). Ordered versions of the bcc structure (D0₃ and B2) are stable to high pressures in Fe–16Si and FeSi (Fischer et al., 2012; Fig. 1c and d). The appearance of the D0₃ structure only in the Fe–16Si phase diagram at high pressures and temperatures may be due to its composition, which is very close to Fe₃Si, having the preferred stoichiometry of the D0₃ structure. The B20 structure appears only in the phase diagram of FeSi, again likely driven by the stoichiometry of this composition.

Fig. 7 shows a series of temperature–composition (T – X) phase diagrams at 50, 80, 125, and 145 GPa, based on the compilation of this study with earlier subsolidus phase diagrams of iron (Komabayashi and Fei, 2010) and Fe–16Si (Fischer et al., 2012). Most of the compositions of triple points shown in Fig. 7 are estimated but are bracketed by the available data. Data from Asanuma et al. (2008) on Fe–3.4Si are shown, but are incompatible with the constraints imposed by other studies. Therefore, in constructing T – X plots we do not match the temperatures reported by Asanuma et al. (2008), only the structures they report as stable at 3.4 wt% silicon. Experiments by Asanuma et al. (2008) likely suffered from large temperature gradients, since the laser-heated spot was similar in size to the X-ray beam. With large temperature gradients and the persistence of the hcp phase outside of equilibrium (such as in the Fe–9Si phase diagram), Asanuma et al. (2008) may have reported coexisting fcc+hcp phases over a wider temperature range than the mixture would occupy at equilibrium. This is supported by Brosh et al. (2009), who were also unable to fit the data of Asanuma et al. (2008) in their thermodynamic modeling of the Fe–FeSi system. Subsolidus data on Fe–Si–Ni alloys are not included in Fig. 7 (e.g., Morard et al., 2011; Sakai et al., 2011) due to uncertain and inconsistent effects of Ni on the crystal structures of these alloys.

Melting points for Fe (Ma et al., 2004); Fe–10Si–5Ni and Fe–15Si–5Ni (Morard et al., 2011); Fe–16Si (Fischer et al., 2012); Fe–18Si (Asanuma et al., 2010); and FeSi (Lord et al., 2010) are also shown in Fig. 7. The melting curve of pure iron predicted by our T – X phase diagrams is similar to or slightly higher than that reported by Ma et al. (2004), but is compatible within uncertainty.

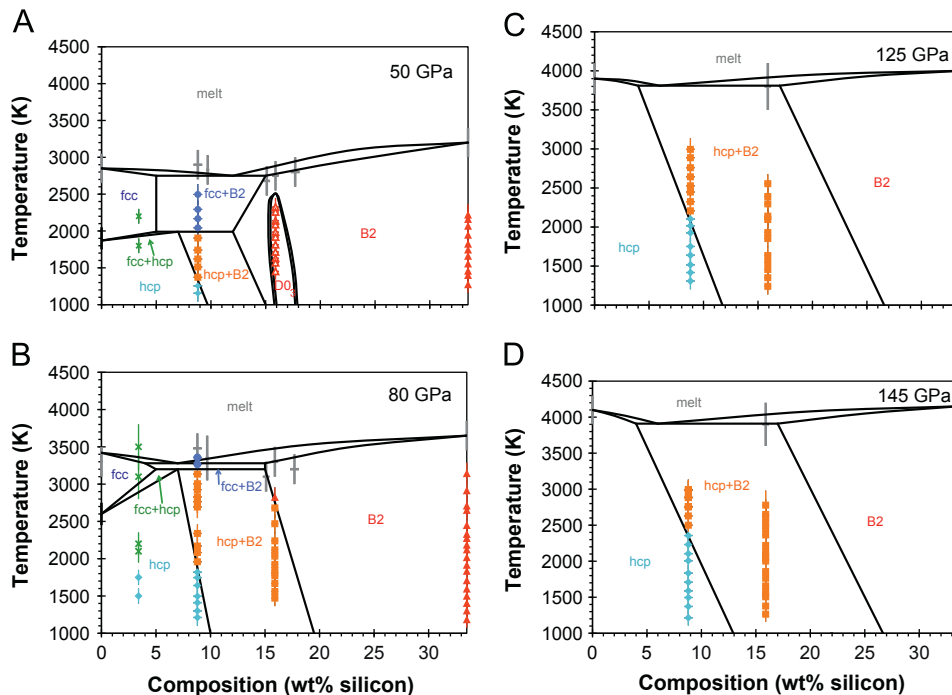


Fig. 7. Composition–temperature phase diagrams in the Fe–FeSi system at varying pressures. (A) 50 GPa, (B) 80 GPa, (C) 125 GPa, and (D) 145 GPa. Gray crosses: melting points. Green \times s: fcc+hcp. Other data symbols are as in Fig. 1. Data points indicate actual constraints on the phase diagrams; black lines (phase boundaries) and triple points are estimated. Some two-phase fields are unlabeled for clarity. Data from three phase regions (fcc+hcp+B2) in Fig. 1 are labeled as fcc+B2 (see text for details). Data are shown for Fe (Komabayashi and Fei, 2010; Ma et al., 2004); Fe–3.4Si (Asanuma et al., 2008); Fe–9Si (this study); Fe–10Si–5Ni and Fe–15Si–5Ni (Morard et al., 2011); Fe–16Si (Fischer et al., 2012); Fe–18Si (Asanuma et al., 2010); and FeSi (this study; Lord et al., 2010). (For interpretation of the references to color in this figure legend, the reader is referred to the web version of this article.)

The melting temperatures that we report for Fe–9Si and Fe–16Si most likely represent solidus temperatures, since the appearance of diffuse scattering probably coincides with the first appearance of melt. As shown in Fig. 7, the melting points of Fe, Fe–9Si, Fe–10Si–5Ni, Fe–15Si–5Ni, Fe–16Si, and Fe–18Si are indistinguishable within uncertainty up to 80 GPa, in contrast to the conclusions of Morard et al. (2011) (also see Fig. S3). This suggests that silicon does not strongly depress the melting point of iron, and that low concentrations of nickel also have no detectable effect. The melting point of FeSi (Lord et al., 2010) is higher than those of the other alloys at lower pressures, but is more similar by 125 GPa (Fig. 7c). This necessitates a narrow phase loop on the iron-rich side of the eutectic, and a fairly narrow phase loop on the FeSi side that shrinks with increasing pressure. However, this interpretation depends on the melting curve of iron chosen as the basis for comparison.

At 50 GPa, the fcc–B2 eutectic lies between 9 and 16 wt% silicon (Fig. 7a), based on the observed structures of the liquidus phases (Si-poor fcc phase for Fe–9Si; Si-rich B2 for Fe–16Si). By 80 GPa, the eutectic has shifted to less than 9 wt% Si, while the fcc+B2 field has shrunk to a narrow region just below the melting point. By 125 GPa, the fcc phase disappears. The eutectic at 125 GPa is between the hcp and B2 phases, located somewhere lower than 16 wt% silicon. The hcp+B2 field exists at all pressures shown in Fig. 7 and expands with increasing pressure. At 50 GPa, the DO_3 structure is stable near stoichiometric Fe_3Si . Fig. 7a depicts this region as not converging with higher temperature phase boundaries, allowing for a single B2 field surrounding it. This type of topology in T – X phase diagrams involving ordering transitions occurs in other systems at 1 bar, such as the Fe–Pt and Co–Pt systems (Massalski, 1986). It is also possible that the DO_3 region lies tangent to the fcc+B2 field, creating two distinct B2 fields at lower pressures. The ordered region shrinks to lower temperatures

with increasing pressure as the DO_3 structure is replaced by the less ordered B2 structure at high temperatures, and is gone from the phase diagram by 80 GPa. Kuwayama and Hirose (2004) reported the existence of a phase with 25.1 wt% silicon at 21 GPa, corresponding to stoichiometric Fe_3Si_2 . However, we do not have data near this composition to evaluate its stability at these higher pressures, so we do not include it in our phase diagrams. Further in situ work is needed to clarify that part of the phase diagram at pressures below 50 GPa. Fig. 7 illustrates that phase diagrams of iron–silicon alloys contain fewer phases at higher pressures. We only report the hcp and B2 structures at 125 and 145 GPa, though other structures may exist at other compositions.

Fig. 8 shows a series of pressure–composition (P – X) phase diagrams at 1500, 1800, 2100, and 2400 K, based on the same datasets shown in Fig. 7, with 1 bar phase relations from Massalski (1986). As in Fig. 7, data from Asanuma et al. (2008) are shown but conflict with the other datasets. While we do predict an fcc+hcp field at 3.4 wt% silicon, it does not generally match the pressures (or equivalently, temperatures) of that study's data. We also include data from Kuwayama et al. (2009) on Fe–6.4Si, which are consistent with our data. Morard et al. (2011) performed a crossing of the hcp+B2 to fcc+B2 boundary in Fe–5Ni–10Si and found a transition at ~ 50 GPa and 2150 K, in agreement with our results (Figs. 1b, 7a, and 8c).

The bcc structure is stable only in a thin lens-shaped field near 1 bar at 1500 K. At 1800 K, this field has shrunk toward the iron-rich, 1 bar corner of the phase diagram, disappearing by 2100 K. The Fe_2Si structure is only stable at low pressures and at 1500 K. As in the T – X plots of Fig. 7, the DO_3 structure is stable over a narrow compositional range but more extended pressure range. Though the width of this field is not precisely constrained, it becomes stable over a smaller pressure range with increasing temperature. As mentioned above, the range of P – T – X stability of

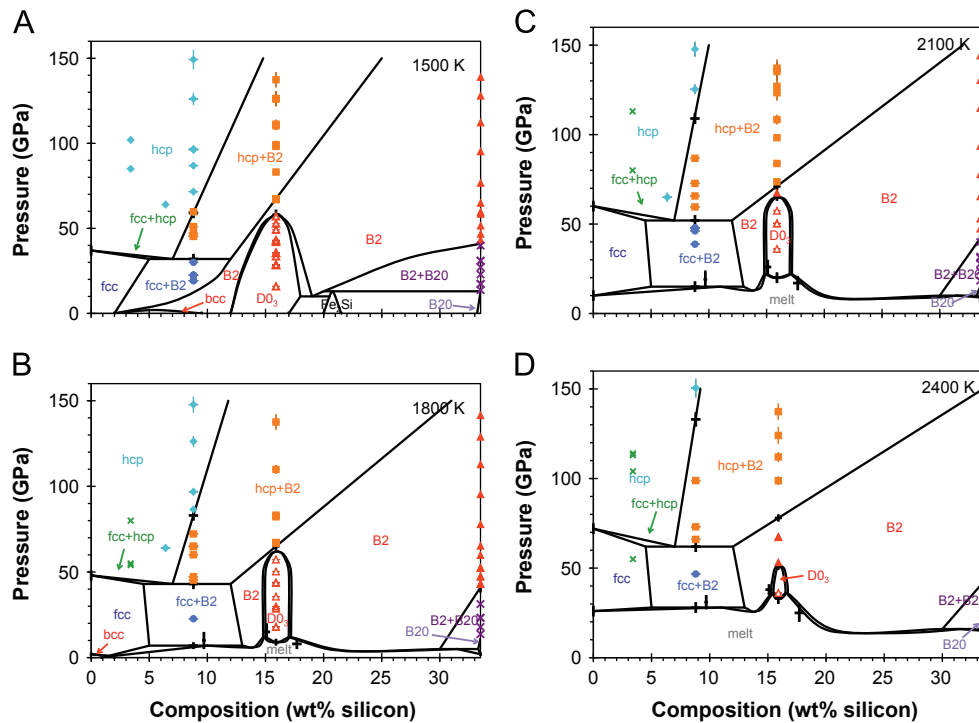


Fig. 8. Composition–pressure phase diagrams in the Fe–FeSi system at varying temperatures. (A) 1500 K, (B) 1800 K, (C) 2100 K, and (D) 2400 K. Symbols are as described in Figs. 1 and 7. Data points indicate actual constraints on the phase diagrams; black lines (phase boundaries) and triple points are estimated. Some two-phase fields are unlabeled for clarity. Black crosses: melting points and other phase boundaries with estimated 1σ uncertainties. Asanuma et al. (2008) do not report uncertainties in pressure (Fe–3.4Si data). References are the same as in Fig. 7, with 1 bar phase relations from Massalski (1986) and data for Fe–6.4Si from Kuwayama et al. (2009).

the Fe_3Si_2 phase discovered by Kuwayama and Hirose (2004) remains uncertain, so this phase is not included in Fig. 8.

The composition of the fcc–hcp–B2 triple point (where the hcp + B2, fcc+hcp, and fcc+B2 fields meet) is only constrained by the available data to fall between 3.4 and 8.8 wt% silicon, so the composition of this triple point is set at 7 wt% Si in Fig. 8. For this case, the hcp+B2 field expands with increasing temperature. The hcp to hcp+B2 and the hcp+B2 to B2 phase boundaries both have positive slopes in P – X space at all temperatures. When extrapolated to higher pressures, Fig. 8 illustrates that alloys containing more silicon than the triple point composition will exist as an hcp + B2 mixture then transform to a pure hcp structure with increasing pressure. This is seen in Fe–9Si at 1500 K and 1800 K (Fig. 8a and b). Conversion from an hcp+B2 mixture to the hcp structure with increasing pressure was predicted for Fe–16Si (Fischer et al., 2012), but the P – X phase diagrams illustrate that this series of transitions should occur for a wide compositional range of Fe–Si alloys extending from ~ 4 to 8 wt% silicon, possibly to FeSi or even more silicon-rich alloys at sufficiently high pressures.

Kuwayama et al. (2009) produced a P – X phase diagram in the Fe–FeSi system at 2100 K. They report an hcp+B2 region with a compositional gap of only 3 wt% silicon based on microprobe analysis of a recovered sample from 61 GPa, but our observation of hcp+B2 mixtures in both Fe–9Si and Fe–16Si requires that the two-phase loop be wider than this (Fig. 8c). This minor discrepancy could be due to Kuwayama et al. (2009) probing an activation volume within their sample that was larger than its grain size, so that their compositional determination for each phase included some averaging over both phases.

Brosh et al. (2009) calculated a P – X phase diagram in the Fe–FeSi system at 300 K. Their results are in approximate agreement with our findings, though they do not differentiate between different bcc-like structures (bcc, B2, and D_{03}). They predict a very wide hcp + B2 compositional gap, extending all the way to FeSi by ~ 130 GPa, which is not incompatible with our phase diagram. However, they

draw an hcp to hcp+B2 boundary whose slope has the opposite sign from ours, where our slope is constrained by data at Fe–9Si and knowledge of the fcc–hcp–B2 triple point location.

4.5. Iron–silicon alloys in the Earth

It has been proposed that FeSi occurs in the Earth's D'' layer, either as a reaction product between silicates and the outer core (Knittle and Jeanloz, 1991), or as an exsolution product of the outer core formed during secular cooling (Buffett et al., 2000). Recovered B2–FeSi is an electrical conductor at 1 bar (Dobson et al., 2002), so Dubrovinsky et al. (2003) proposed that B2–FeSi could explain the electrically conductive layer at the base of Earth's mantle (e.g., Buffett, 1992). Based on our phase diagram (Fig. 1d), FeSi at these pressures should have the B2 structure. Since our melting data are consistent with those of Lord et al. (2010), we similarly conclude that solid FeSi could be stable within some region of the D'' layer, with the thickness and depth of this region depending on the thermal structure of the D'' layer.

The melting curve of Fe–9Si can be used to constrain core temperatures, for a core of this composition. Using the Simon equation parameterization, we can extrapolate to melting at core–mantle boundary (CMB) conditions (136 GPa), finding a melting point of 4380 K. This is a minimum core temperature, if the outer core is Fe–9Si alloy. There may be a kink in the melting curve where it intersects the hcp+B2 to fcc+B2 phase boundary at ~ 110 GPa; this would raise the melting temperature at 136 GPa. We can also extrapolate the melting curve of Fe–9Si to the inner core boundary (329 GPa), finding a temperature of 6650 K. However, this calculation requires very large extrapolations in pressure and temperature, and neglects phase transitions in the solid that could change the melting curve.

Silicon is relatively inefficient at depressing the melting point of iron-rich alloys at core pressures (Figs. 7 and S3). The light element in Earth's core is thought to depress the melting point by

~700–1100 K at core conditions (Anderson, 1998), but our results show that silicon may be a poor candidate for this. The melting point of Fe–FeSi alloys is no more than ~200 K less than that of pure iron (Ma et al., 2004) at 70–80 GPa, for example. This is less than the ~500 K melting point depression in the Fe–FeO system (Fischer and Campbell, 2010; Seagle et al., 2008) and the 1000–1100 K depression in the Fe–S system (Campbell et al., 2007) at similar pressures relative to the iron melting curve of Ma et al. (2004). Comparing to a different melting curve of iron changes these numbers (Fig. S3), but does not change the relative differences in melting point depression for these various elements. An Fe–Si core would therefore require higher temperatures than an Fe–S or Fe–O core. The melting curve of Fe–9Si is also much steeper than the slope of the iron–sulfide eutectic (Campbell et al., 2007), and somewhat steeper than that of the Fe–FeO eutectic (Seagle et al., 2008), so an Fe–Si core would crystallize more slowly and drive compositional convection less efficiently for a given cooling rate.

Our phase diagrams in the Fe–FeSi system can be used to determine which phases are stable in the Earth's core. Fig. 7d illustrates a *T*–*X* phase diagram near core–mantle boundary pressures. It shows that for a compositional range spanning at least 9–16 wt% Si, an hcp+B2 mixture is the stable assemblage at temperatures near melting in the outer core. We find approximately the same slope for the hcp to hcp+B2 phase boundary as Lin et al. (2009) and Kuwayama et al. (2009) (Fig. S2), though our denser *P*–*T* coverage resolves a slight curvature of the phase boundary at high pressures. Extrapolating these phase boundaries to 329 GPa, Fe–9Si will exist as a mixture of hcp and B2 phases for an inner core boundary temperature greater than ~3500 K (Fig. S2), whereas the phase boundaries of Lin et al. (2009) and Kuwayama et al. (2009) require higher temperatures for the B2 phase to be stable. However, there is a high degree of uncertainty inherent to such large extrapolations of phase diagrams. At temperatures closer to 6650 K, the phase loop is much wider, and an inner core alloy containing 6–8 wt% Si (Brosh et al., 2009; Fischer et al., 2012) or less will also exist as an hcp+B2 mixture at inner core pressures, in agreement with the results of Brosh et al. (2009) and Dubrovinsky et al. (2003). The possibility of a two-phase mixture in Earth's inner core should motivate future studies on the thermal evolution, geodynamics, and anisotropy of a heterogeneous core. For example, an iron-rich alloy may begin crystallizing as an hcp+B2 mixture, but evolve to crystallize a pure hcp structure as secular cooling proceeds, depending on the composition, thermal history, and temperature structure of the core. This could relate to layered anisotropy variations in the inner core (e.g., Deguen, 2012; Mattesini et al., 2010).

The effect of nickel on the melting point of Fe–Si alloys appears negligible within the resolution of our data and that of Morard et al. (2011) (Figs. 6–8). Effects of nickel on the crystal structures of iron–silicon alloys are unclear (e.g., Kuwayama et al., 2008), but recent studies suggest that Fe–Si alloys with ~5–10 wt% nickel have the hcp structure at inner core pressures and room temperature (Asanuma et al., 2011; Sakai et al., 2011). Further study on Fe–Ni–Si alloys at high pressures and temperatures is needed to clarify effects of nickel on the phase diagram at inner core conditions.

5. Conclusions

The pressure–temperature phase diagrams of Fe–9Si and stoichiometric FeSi have been determined to high temperatures and pressures using synchrotron X-ray diffraction. The phase diagram of Fe–9Si reported here is similar to those of prior studies (Kuwayama et al., 2009; Lin et al., 2002), although a melting curve had not previously been determined for this composition.

The Fe–9Si phase diagram also includes the B2 crystal structure, representing a higher degree of ordering than the bcc structure reported previously (Lin et al., 2002, 2009). In situ study of the B20–B2 phase transition in FeSi shows a wide two-phase region where these structures coexist, completely converting to the B2 structure at higher pressures. At the highest pressures reached in this study, Fe–FeSi phase diagrams become simpler, containing only the hcp and B2 structures. Alloys containing more than ~4–8 wt% silicon will convert to an hcp+B2 mixture, and later to the hcp structure, with increasing pressure. For a postulated Earth's core comprised of Fe–Si alloy, 4380 K is a minimum outer core temperature, based on the eutectic melting point of Fe–9Si. Melting temperatures of Fe–FeSi alloys are very similar at core conditions, indicating that silicon is inefficient at depressing the melting point of iron. For Fe–Si alloys with plausible inner core compositions, our phase diagrams suggest the stability of an hcp+B2 mixture under *P*–*T* conditions of the Earth's inner core.

Acknowledgments

We thank the two anonymous reviewers for their comments and the editor for handling our manuscript. We wish to acknowledge Jason Knight, Alastair MacDowell, and Jinyuan Yan, beamline scientists who helped us during this project. We would like to thank Maria Valdes for help with sample preparation, Sergey Tkachev for assistance with gas-loading, and Bethany Chidester, Gwen Gage, and Hannah Mark for their assistance at the beamline. This material is based upon work supported by a National Science Foundation (NSF) Graduate Research Fellowship to R.A.F. This work was also supported by the NSF by Grant EAR-0847217 to A.J.C. and by Grant EAR-0944298 to D.L.H. Portions of this work were performed at GeoSoilEnviroCARS (Sector 13), Advanced Photon Source (APS), Argonne National Laboratory. GeoSoilEnviroCARS is supported by the NSF—Earth Sciences (EAR-0622171) and the Department of Energy (DOE)—Geosciences (DE-FG02-94ER14466). Use of the APS was supported by the U.S. DOE, Office of Science, Office of Basic Energy Sciences, under Contract no. DE-AC02-06CH11357. This research was partially supported by COMPRES, the Consortium for Materials Properties Research in Earth Sciences under NSF Cooperative Agreement EAR 10-43050. The Advanced Light Source is supported by the Director, Office of Science, Office of Basic Energy Sciences, of the U.S. DOE under Contract no. DE-AC02-05CH11231.

Appendix A. Supplementary materials

Supplementary data associated with this article can be found in the online version at <http://dx.doi.org/10.1016/j.epsl.2013.04.035>.

References

- Alfè, D., Gillan, M.J., Price, G.D., 2002. Composition and temperature of the Earth's core constrained by combining ab initio calculations and seismic data. *Earth Planet. Sci. Lett.* 195, 91–98.
- Allègre, C.J., Poirier, J.-P., Humler, E., Hofmann, A.W., 1995. The chemical composition of the Earth. *Earth Planet. Sci. Lett.* 134, 515–526.
- Anderson, O.L., 1998. The Grüneisen parameter for iron at outer core conditions and the resulting conductive heat and power in the core. *Phys. Earth Planet. Inter.* 109, 179–197.
- Antonangeli, D., Siebert, J., Badro, J., Farber, D.L., Fiquet, G., Morard, G., Ryerson, F.J., 2010. Composition of the Earth's inner core from high-pressure sound velocity measurements in Fe–Ni–Si alloys. *Earth Planet. Sci. Lett.* 295, 292–296.
- Asanuma, H., Ohtani, E., Sakai, T., Terasaki, H., Kamada, S., Hirao, N., Sata, N., Ohishi, Y., 2008. Phase relations of Fe–Si alloy up to core conditions: implications for the Earth inner core. *Geophys. Res. Lett.* 35, L12307.
- Asanuma, H., Ohtani, E., Sakai, T., Terasaki, H., Kamada, S., Kondo, T., Kikegawa, T., 2010. Melting of iron–silicon alloy up to the core–mantle boundary pressure:

- implications to the thermal structure of the Earth's core. *Phys. Chem. Miner.* 37, 353–359.
- Asanuma, H., Ohtani, E., Sakai, T., Terasaki, H., Kamada, S., Hirao, N., Ohishi, Y., 2011. Static compression of $\text{Fe}_{0.83}\text{Ni}_{0.09}\text{Si}_{0.08}$ alloy to 374 GPa and $\text{Fe}_{0.93}\text{Si}_{0.07}$ alloy to 252 GPa: implications for the Earth's inner core. *Earth Planet. Sci. Lett.* 310, 113–118.
- Balchan, A.S., Cowan, G.R., 1966. Shock compression of two iron–silicon alloys to 2.7 megabars. *J. Geophys. Res.* 71, 3577–3588.
- Birch, F., 1952. Elasticity and constitution of the Earth's interior. *J. Geophys. Res.* 37, 227–286.
- Brosh, E., Makov, G., Shneck, R.Z., 2009. Thermodynamic analysis of high-pressure phase equilibria in Fe–Si alloys, implications for the inner-core. *Phys. Earth Planet. Inter.* 172, 289–298.
- Buffett, B.A., 1992. Constraints on magnetic energy and mantle conductivity from the forced nutations of the Earth. *J. Geophys. Res.* 97, 19581–19597.
- Buffett, B.A., Garnero, E.J., Jeanloz, R., 2000. Sediments at the top of Earth's core. *Science* 17, 1338–1342.
- Campbell, A.J., Seagle, C.T., Heinz, D.L., Shen, G., Prakapenka, V.B., 2007. Partial melting in the iron–sulfur system at high pressure: a synchrotron X-ray diffraction study. *Phys. Earth Planet. Inter.* 162, 119–128.
- Campbell, A.J., Danielson, L., Richter, K., Seagle, C.T., Wang, Y., Prakapenka, V.B., 2009. High pressure effects on the iron–iron oxide and nickel–nickel oxide oxygen fugacity buffers. *Earth Planet. Sci. Lett.* 286, 556–564.
- Caracas, R., Wentzcovitch, R., 2004. Equation of state and elasticity of FeSi. *Geophys. Res. Lett.* 31, L20603.
- Côté, A.S., Vočadlo, L., Dobson, D.P., Alfè, D., Brodholt, J.P., 2010. Ab initio lattice dynamics calculations on the combined effect of temperature and silicon on the stability of different iron phases in the Earth's inner core. *Phys. Earth Planet. Inter.* 178, 2–7.
- Deguen, R., 2012. Structure and dynamics of Earth's inner core. *Earth Planet. Sci. Lett.* 333–334, 211–225.
- Dewaele, A., Loubeyre, P., Ocellli, F., Mezouar, M., Dorogokupets, P.I., Torrent, M., 2006. Quasihydrostatic equation of state of iron above 2 Mbar. *Phys. Rev. Lett.* 97, 215504.
- Dewaele, A., Mezouar, M., Guignot, N., Loubeyre, P., 2007. Melting of lead under high pressure studied using second-scale time-resolved x-ray diffraction. *Phys. Rev. B* 76, 144106.
- Dobson, D.P., Vočadlo, L., Wood, I.G., 2002. A new high-pressure phase of FeSi. *Am. Mineral.* 87, 784–787.
- Dobson, D.P., Crichton, W.A., Bouvier, P., Vočadlo, L., Wood, I.G., 2003. The equation of state of CsCl-structured FeSi to 40 GPa: implications for silicon in the Earth's core. *Geophys. Res. Lett.* 30, 1014.
- Dubrovinsky, L., Dubrovinskaya, N., Langenhorst, F., Dobson, D., Rubie, D., Gessmann, C., Abrikosov, I.A., Johansson, B., Baykov, V.I., Vitos, L., Le Bihan, T., Crichton, W.A., Dmitriev, V., Weber, H.-P., 2003. Iron–silica interaction at extreme conditions and the electrically conducting layer at the base of Earth's mantle. *Nature* 422, 58–61.
- Fei, Y., Ricolleau, A., Frank, M., Mibe, K., Shen, G., Prakapenka, V., 2007. Toward an internally consistent pressure scale. *Proc. Natl. Acad. Sci. USA* 104, 9182–9186.
- Fischer, R.A., Campbell, A.J., 2010. High-pressure melting of wüstite. *Am. Mineral.* 95, 1473–1477.
- Fischer, R.A., Campbell, A.J., Shofner, G.A., Lord, O.T., Dera, P., Prakapenka, V.B., 2011. Equation of state and phase diagram of FeO. *Earth Planet. Sci. Lett.* 304, 496–502.
- Fischer, R.A., Campbell, A.J., Caracas, R., Reaman, D.M., Dera, P., Prakapenka, V.B., 2012. Equation of state and phase diagram of Fe–16Si alloy as a candidate component of Earth's core. *Earth Planet. Sci. Lett.* 357–358, 268–276.
- Guyot, F., Zhang, J., Martinez, I., Matas, J., Ricard, Y., Javoy, M., 1997. *P–V–T* measurements of iron silicide (ϵ -FeSi): implications for silicate–metal interactions in the early Earth. *Eur. J. Mineral.* 9, 277–285.
- Hammersley, A.P., Svensson, S.O., Hanfland, M., Fitch, A.N., Hausermann, D., 1996. Two-dimensional detector software: from real detector to idealized image or two-theta scan. *High Pressure Res.* 14, 235–248.
- Heinz, D.L., Jeanloz, R., 1987. Temperature measurement in the laser-heated diamond anvil cell. In: Manghnani, M.H. and Syono, Y. (Eds.), *High-Pressure Research in Mineral Physics*, Terra Scientific Publishing, Tokyo / American Geophysical Union, Washington, pp. 113–127.
- Hirao, N., Ohtani, E., Kondo, T., Kikegawa, B., 2004. Equation of state of iron–silicon alloys to megabar pressure. *Phys. Chem. Miner.* 31, 329–336.
- Javoy, M., Kaminski, E., Guyot, F., Andrault, D., Sanloup, C., Moreira, M., Labrosse, S., Jambon, A., Agrinier, P., Davaille, A., Jaupart, C., 2010. The chemical composition of the Earth: enstatite chondrite models. *Earth Planet. Sci. Lett.* 293, 259–268.
- Knittle, E., Jeanloz, R., 1991. Earth's core–mantle boundary: results of experiments at high pressures and temperatures. *Science* 251, 1438–1443.
- Knittle, E., Williams, Q., 1995. Static compression of ϵ -FeSi and an evaluation of reduced silicon as a deep Earth constituent. *Geophys. Res. Lett.* 22, 445–448.
- Komabayashi, T., Fei, Y., Meng, Y., Prakapenka, V., 2009. In-situ X-ray diffraction measurements of the γ – ϵ transition boundary of iron in an internally-heated diamond anvil cell. *Earth Planet. Sci. Lett.* 282, 252–257.
- Komabayashi, T., Fei, Y., 2010. Internally consistent thermodynamic database for iron to the Earth's core conditions. *J. Geophys. Res.* 115, B03202.
- Kunz, M., MacDowell, A.A., Caldwell, W.A., Cambie, D., Celestre, R.S., Domning, E.E., Duarte, R.M., Gleason, A.E., Glossinger, J.M., Kelez, N., Plate, D.V., Yu, T., Zaig, J. M., Padmore, H.W., Jeanloz, R., Alivisatos, A.P., Clark, S.M., 2005. A beamline for high-pressure studies at the Advanced Light Source with a superconducting bending magnet as the source. *J. Synchrotron Radiat.* 12, 650–658.
- Kuwayama, Y., Hirose, K., 2004. Phase relations in the system Fe–FeSi at 21 GPa. *Am. Mineral.* 89, 273–276.
- Kuwayama, Y., Hirose, K., Sata, N., Ohishi, Y., 2008. Phase relations of iron and iron–nickel alloys up to 300 GPa: implications for composition and structure of the Earth's inner core. *Earth Planet. Sci. Lett.* 273, 379–385.
- Kuwayama, Y., Sawai, T., Hirose, K., Sata, N., Ohishi, Y., 2009. Phase relations of iron–silicon alloys at high pressure and high temperature. *Phys. Chem. Miner.* 36, 511–518.
- Lin, J.-F., Heinz, D.L., Campbell, A.J., Devine, J.M., Shen, G., 2002. Iron–silicon alloy in Earth's core? *Science* 295, 313–315.
- Lin, J.-F., Campbell, A.J., Heinz, D.L., Shen, G., 2003. Static compression of iron–silicon alloys: implications for silicon in the Earth's core. *J. Geophys. Res.* 108, 2045.
- Lin, J.-F., Scott, H.P., Fischer, R.A., Chang, Y.-Y., Kantor, I., Prakapenka, V.B., 2009. Phase relations of Fe–Si alloy in Earth's core. *Geophys. Res. Lett.* 36, L06306.
- Lord, O.T., Walter, M.J., Dobson, D.P., Armstrong, L., Clark, S.M., Klepe, A., 2010. The FeSi phase diagram to 150 GPa. *J. Geophys. Res.* 115, B06208.
- Ma, Y., Somayazulu, M., Shen, G., Mao, H.-K., Shu, J., Hemley, R.J., 2004. In situ X-ray diffraction studies of iron to Earth-core conditions. *Phys. Earth Planet. Inter.* 143–144, 455–467.
- Mao, H.K., Xu, J., Bell, P.M., 1986. Calibration of the ruby pressure gauge to 800 kbar under quasi-hydrostatic conditions. *J. Geophys. Res.* 91, 4673–4676.
- Massalski, T.B., 1986. *Binary Alloy Phase Diagrams*. American Society for Metals, Metals Park, Ohio.
- Matteini, M., Belonoshko, A.B., Bufo, E., Ramírez, M., Simak, S.I., Udías, A., Mao, H.-K., Ahuja, R., 2010. Hemispherical anisotropic patterns of the Earth's inner core. *Proc. Natl. Acad. Sci. USA* 107, 9507–9512.
- McDonough, W.F., 2003. Compositional model for the Earth's core. In: Carlson, R.W. (Ed.), *Treatise of Geochemistry*, vol. 2. Elsevier-Pergamon, Oxford, pp. 547–568.
- Miller, N.A., 2009. *Melting and Phase Relations in Iron–Silicon Alloys With Applications to the Earth's Core* (M.S. thesis). University of Maryland, College Park.
- Morard, G., Andrault, D., Guignot, N., Sanloup, C., Mazouar, M., Petitgirard, S., Fiquet, G., 2008. In-situ determination of Fe–Fe₃S phase diagram and liquid structural properties up to 65 GPa. *Earth Planet. Sci. Lett.* 272, 620–626.
- Morard, G., Andrault, D., Guignot, N., Siebert, J., Garbarino, G., Antonangeli, D., 2011. Melting of Fe–Ni–Si and Fe–Ni–S alloys at megabar pressures: implications for the core–mantle boundary temperature. *Phys. Chem. Miner.* 38, 767–776.
- Ono, S., Kikegawa, T., Ohishi, Y., 2007. Equation of state of the high-pressure polymorph of FeSi to 67 GPa. *Eur. J. Mineral.* 19, 183–187.
- Poirier, J.P., 1994. Light elements in the Earth's outer core: a critical review. *Phys. Earth Planet. Inter.* 85, 319–337.
- Prakapenka, V.B., Shen, G., Dubrovinsky, L.S., 2003. Carbon transport in diamond anvil cell. *High Temp.–High Pressure* 35/36, 237–249.
- Prakapenka, V.B., Kuba, A., Kuznetsov, A., Laskin, A., Shkurikhin, O., Dera, P., Rivers, M.L., Sutton, S.R., 2008. Advanced flat top laser heating system for high pressure research at GSECARS: application to the melting behavior of germanium. *High Pressure Res.* 28, 225–235.
- Ricolleau, A., Fei, Y., Corgne, A., Siebert, J., Badro, J., 2011. Oxygen and silicon contents of Earth's core from high pressure metal–silicate partitioning experiments. *Earth Planet. Sci. Lett.* 310, 409–421.
- Ringwood, A.E., 1959. On the chemical evolution and densities of the planets. *Geochim. Cosmochim. Acta* 15, 257–283.
- Rivers, M., Prakapenka, V.B., Kubo, A., Pullins, C., Holl, C.M., Jacobsen, S.D., 2008. The COMPRES/GSECARS gas-loading system for diamond anvil cells at the Advanced Photon Source. *High Pressure Res.* 28, 273–292.
- Rubie, D.C., Frost, D.J., Mann, U., Asahara, Y., Nimmo, F., Tsuno, K., Kegler, P., Holzheid, A., Palme, H., 2011. Heterogeneous accretion, composition and core–mantle differentiation of the Earth. *Earth Planet. Sci. Lett.* 301, 31–42.
- Sakai, T., Ohtani, E., Hirao, N., Ohishi, Y., 2011. Stability field of the hcp-structure for Fe, Fe–Ni, and Fe–Ni–Si alloys up to 3 Mbar. *Geophys. Res. Lett.* 38, L09302.
- Santamaría-Pérez, D., Boehler, R., 2008. FeSi melting curve up to 70 GPa. *Earth Planet. Sci. Lett.* 265, 743–747.
- Sata, N., Hirose, K., Shen, G., Nakajima, Y., Ohishi, Y., Hirao, N., 2010. Compression of FeSi, Fe₃C, Fe_{0.95}O, and Fe under the core pressures and implication for light element in the Earth's core. *J. Geophys. Res.* 115, B09204.
- Seagle, C.T., Heinz, D.L., Campbell, A.J., Prakapenka, V.B., Wanless, S.T., 2008. Melting and thermal expansion in the Fe–FeO system at high pressure. *Earth Planet. Sci. Lett.* 265, 655–665.
- Shahar, A., Ziegler, K., Young, E.D., Ricolleau, A., Schauble, E.A., Fei, Y., 2009. Experimentally determined Si isotope fractionation between silicate and Fe metal and implications for Earth's core formation. *Earth Planet. Sci. Lett.* 288, 228–234.
- Shen, G., Rivers, M.L., Wang, Y., Sutton, S.R., 2001. Laser heated diamond cell system at the Advanced Photon Source for *in situ* measurements at high pressure and temperature. *Rev. Sci. Instrum.* 72, 1273–1282.
- Shen, G., Rivers, M.L., Wang, Y., Sutton, S.R., 2005. Facilities for high-pressure research with the diamond anvil cell at GSECARS. *J. Synchrotron Radiat.* 12, 642–649.
- Simon, F., Glatzel, G., 1929. Bemerkungen zur Schmelzdruckkurve. *Z. Anorg. Allg. Chem.* 178, 309–316.
- Stixrude, L., Cohen, R.E., 1995. High-pressure elasticity of iron and anisotropy of Earth's inner core. *Science* 267, 1972–1975.
- Tateno, S., Hirose, K., Ohishi, Y., Tatsumi, Y., 2010. The structure of iron in Earth's inner core. *Science* 330, 359–361.

- Vočadlo, L., Price, G.D., Wood, I.G., 1999. Crystal structure, compressibility and possible phase transitions in ϵ -FeSi studied by first-principles pseudopotential calculations. *Acta Crystallogr. Sect. B: Struct. Sci.* 55, 484–493.
- Whitaker, M.L., Liu, W., Liu, Q., Wang, L., Li, B., 2008. Combined *in situ* synchrotron X-ray diffraction and ultrasonic interferometry study of ϵ -FeSi at high pressure. *High Pressure Res.* 28, 385–395.
- Whitaker, M.L., Liu, W., Liu, Q., Wang, L., Li, B., 2009. Thermoelasticity of ϵ -FeSi to 8 GPa and 1273 K. *Am. Mineral.* 94, 1039–1044.
- Zhang, J., Guyot, F., 1999a. Thermal equation of state of iron and $\text{Fe}_{0.91}\text{Si}_{0.09}$. *Phys. Chem. Miner.* 26, 206–211.
- Zhang, J., Guyot, F., 1999b. Experimental study of the bcc–fcc phase transformations in the Fe-rich system Fe–Si at high pressures. *Phys. Chem. Miner.* 26, 419–424.
- Zhang, F., Oganov, A.R., 2010. Iron silicides at pressures of the Earth's inner core. *Geophys. Res. Lett.* 37, L02305.